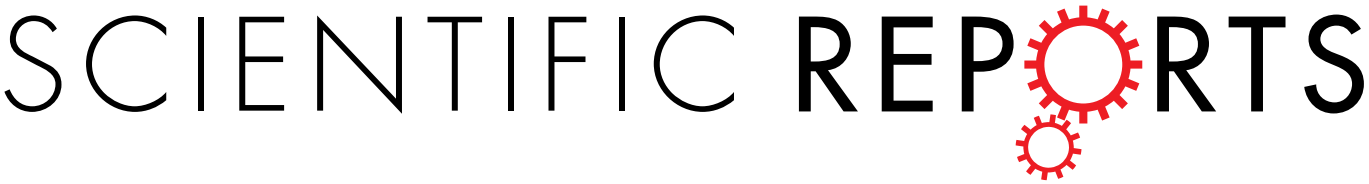

OPEN

High-Performance Solid-State Thermionic Energy Conversion Based on 2D van der Waals Heterostructures: A First-Principles Study

Received: 7 March 2018
Accepted: 25 May 2018
Published online: 18 June 2018

Xiaoming Wang[1,2], Mona Zebarjadi[3,4] & Keivan Esfarjani[4,5,6]

Two-dimensional (2D) van der Waals heterostructures (vdWHs) have shown multiple functionalities with great potential in electronics and photovoltaics. Here, we show their potential for solid-state thermionic energy conversion and demonstrate a designing strategy towards high-performance devices. We propose two promising thermionic devices, namely, the p-type Pt-G-WSe_2-G-Pt and n-type Sc-WSe_2-$MoSe_2$-WSe_2-Sc. We characterize the thermionic energy conversion performance of the latter using first-principles *GW* calculations combined with real space Green's function (GF) formalism. The optimal barrier height and high thermal resistance lead to an excellent performance. The proposed device is found to have a room temperature equivalent figure of merit of 1.2 which increases to 3 above 600 K. A high performance with cooling efficiency over 30% of the Carnot efficiency above 450 K is achieved. Our designing and characterization method can be used to pursue other potential thermionic devices based on vdWHs.

Solid-state thermionic energy conversion was proposed by Mahan *et al.*[1,2] and Shakouri *et al.*[3] about 20 years ago. Working as refrigerators or power generators, they are competitive to[4,5], or could be even better than[6] thermoelectric modules. We note that the key to distinguish the thermionic and thermoelectric devices is the carrier transport regime. While the former is dominated by ballistic transport, the latter operate in the diffusive regime. In ballistic transport, the transport channel is shorter than the electron mean free path. Therefore, the dimension along the transport direction should be at nanoscale (electron mean free path) to meet the requirement of the ballistic transport for the thermionic devices. Solid-state thermionic devices have several advantages over their vacuum counterpart including lower operating temperatures, absence of space charge effect, easy access to cathode and anode for the purpose of cooling and heating and finally higher reliability and easier fabrication due to the absence of the vacuum. The main drawback of the solid-state thermionic modules is the heat leakage through the lattice vibrations of the semiconductor barrier layers, which is much stronger compared to the radiation heat leak in vacuum thermionic modules[7]. Hence, semiconductors with large thermal resistance and large thermal contact resistance are desirable to achieve high device performance, e.g., the cooling efficiency of about 30% can be achieved with the thermal resistance parameter T_R of 200–300 K^1 which is equivalent to a thermal conductance C_{th} of 4–9 MW m^{-2} K^{-1}. Such small thermal conductance values at nanoscale (<100 nm) can be obtained with the emergence of van der Waals heterostructures (vdWHs) composed of vertically stacked two-dimensional (2D) materials[8,9]. For example, we calculated C_{th} to be 4–6 MW m^{-2} K^{-1} for graphene-phosphorene-graphene vdWH sandwiched by gold electrodes[10]. In another work[11] a C_{th} as low as 0.5 MW m^{-2} K^{-1} was experimentally

[1]Department of Physics and Astronomy, The University of Toledo, Toledo, Ohio, 43606, United States. [2]Wright Center for Photovoltaic Innovation and Commercialization, The University of Toledo, Toledo, Ohio, 43606, United States. [3]Department of Electrical and Computer Engineering, University of Virginia, Charlottesville, Virginia, 22904, United States. [4]Department of Materials Science, University of Virginia, Charlottesville, Virginia, 22904, United States. [5]Department of Mechanical and Aerospace Engineering, and University of Virginia, Charlottesville, Virginia, 22904, United States. [6]Department of Physics, University of Virginia, Charlottesville, Virginia, 22904, United States. Correspondence and requests for materials should be addressed to K.E. (email: k1@virginia.edu)

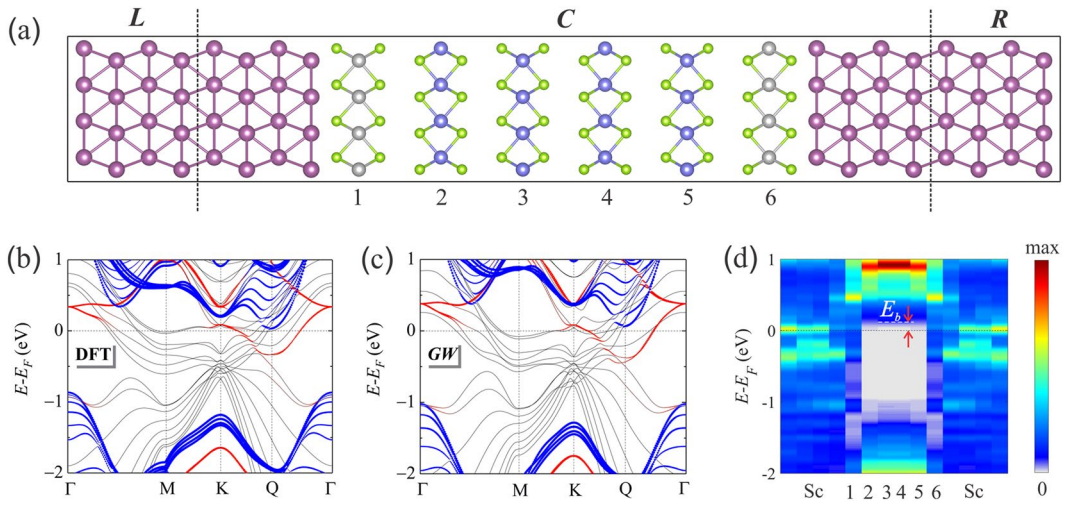

Figure 1. (**a**) Ball-stick model of the proposed device configuration. *L* and *R* are two semi-infinite scandium leads, served as both electron reservoirs and heat sinks. *C* is the scattering region for charge and energy transport. The red, green, gray, and blue balls refer to the Sc, Se, W, and Mo atoms, respectively. The numbers label the different 2D material layers. Fatbands of the scattering region calculated by (**b**) DFT and (**c**) *GW*. The black, red, and blue curves are the bands projected on the Sc layers, the WSe_2 layers labeled 1 and 6, and the $MoSe_2$ layers labeled 2–5, respectively. (**d**) Contour plot of the LDOS calculated by *GW*. The horizontal axis shows the positions of different layers.

estimated for a graphene-WSe_2-graphene vdWH. A molecular dynamics study[12] evaluated a slightly higher C_{th} of 17 MW m^{-2} K^{-1} for both graphene-WSe_2-graphene and graphene-$MoSe_2$-graphene vdWHs. The unprecedented low thermal conductance has renewed interests in solid-state thermionic energy conversion of vdWHs in recent years[10,12–14].

Most of theoretical work on thermionic energy conversion uses the Richardson's law for the thermionic current $J = AT^2e^{-E_b/k_BT}$, where $A = em^*k_B^2\overline{\tau}/(2\pi^2\hbar^3)$ is the Richardson constant, e is the electron charge, m^* is the electron effective mass, $\overline{\tau}$ is the averaged electron transmission denoting the fraction of electrons transmitted from the metal to the semiconductor, k_B is the Boltzmann constant, $\hbar$ is the reduced Planck constant, T is the absolute temperature, and E_b is the thermionic barrier height which is usually taken as a parameter to optimize the thermionic energy conversion efficiency[1,2,12]. A small E_b of several k_BT is found to be optimal for a single barrier thermionic energy converter[1].

In the case of 2D vdWHs, one can benefit from the large database of 2D semiconductors with different electron affinity[15]. In addition, due to quantum confinement effects, 2D materials have layer-dependent band alignment[16]. Therefore, one can tune E_b by changing the number of layers. However, evaluating E_b of the vdWH-based thermionic device is nontrivial due to the Fermi level pinning effect at the metal-2D material interface[17]. The interfacial property also affects $\overline{\tau}$ and C_{th}, both of which are interface dependent and cannot be estimated easily. We note that all the above mentioned difficulties can be remedied by the parameter-free density functional theory (DFT) based first-principles calculations. First-principles study of solid-state thermionic energy conversion, though rarely reported[10], holds great potential in the field due to the strong predictive power of DFT.

A great challenge for DFT to calculate the thermionic transport in vdWHs is to accurately evaluate E_b, which is directly related to the bandgap of the semiconductor layer. DFT usually underestimates the semiconductor bandgap due to the self-interaction error. In addition, the bandgap of 2D materials shows large renormalization due to the substrate or dielectric screening[18–20], a dynamic polarization effect not captured by DFT[21]. This would overestimate the bandgap. The two effects seem to cancel each other to some extent but not completely. The accurate calculation of E_b is of great importance since the thermionic current changes exponentially with E_b and therefore the device performance is quite sensitive to E_b. To this end, we use the *GW* approximation[22] to calculate the quasiparticle band structures and the band alignment of the vdWHs.

We have scanned a series of vdWHs using first-principles calculations and found two promising structures to have the potential for high performance. In particular, we characterize the thermionic energy conversion performance of one of the devices, namely, the Sc-WSe_2-$MoSe_2$-WSe_2-Sc, as shown in Fig. 1(a). We predict an equivalent figure of merit, ZT of 3 at temperatures above 600 K for the proposed device and a high cooling performance with the cooling efficiency over 30% of the Carnot efficiency above 450 K.

Results

Design principles towards high-performance solid-state thermonics based on vdWHs. There are two crucial factors which can lead to good solid-state thermionic devices: low thermal conductance and suitable thermionic barrier height within several k_BT. The former is satisfied in vdWHs due to their weak bonding. The thermal conductance can be further reduced by selecting 2D materials with heavier atomic masses. Therefore, WSe_2, with record low cross-plane thermal conductivity[23], is a good candidate. The second factor, the barrier

WSe_2 layers	barrier type	Al	Ag	Pd	Pt	Au	Au/G	Pt/G
3	p	0.82	0.70	0.59	0.53	0.49	0.28	0.04
	n	0.51	0.31	0.80	0.72	0.53	0.93	1.13
5	p	0.63	0.58	0.51	0.42	0.37	0.22	0.02
	n	0.40	0.30	0.67	0.68	0.53	0.86	1.04

Table 1. PBE barrier heights of the metal-WSe_2-metal configurations. G denotes graphene which covers the metal surface, so the corresponding configuration is metal-G-WSe_2-G-metal. All the numbers are in eV.

height, can be tuned by either using different metal electrodes with different work functions or changing the number of WSe_2 layers to tune the electron affinity due to the quantum confinement effect. Note that, we should avoid using too thin WSe_2 layers, namely, mono- or bilayer WSe_2, to avoid the quantum tunneling effect, which would degrade the device performance. On the other hand, too thick WSe_2 layers are also not preferred due to the requirement of the ballistic transport. Anderson's rule, which is a simple and approximate method to estimate the band alignment, does not always predict the correct barrier height[10]. The strong Fermi level pinning effect in 2D materials[17] rules out this simple method. Therefore, we evaluate the band alignment between WSe_2 and several metals in the metal-WSe_2-metal configuration from DFT calculations. During the calculations, the in-plane lattice parameters of the metals (<111> surfaces are used.) are adapted to that of the WSe_2 layer while the cross-plane lattices are relaxed using the van der Waals functional (methods section). Both the n-type and p-type barrier heights, defined as $E_b^n = CBM - E_F$ and $E_b^p = E_F - VBM$ where CBM and VBM stands for the conduction band minimum and valence band maximum of the WSe_2 layers, are summarized in Table 1. As can be seen, the barrier heights with all the metals considered in the metal-WSe_2-metal configurations are large both for electron and hole transport. The work functions of the metals span a range from 4.2 eV of Al to 6.1 eV of Pt. The ionization potential (IP) of WSe_2 is calculated to be 4.9 eV. Therefore, Anderson's rule which would predict ohmic contact for Pt, would not be true according to our calculations. Increasing the WSe_2 layer thickness would reduce the barrier height which is however still too high for 5 layers. Further increase of the WSe_2 layer thickness could reduce the barrier height. But thick barriers will violate the ballistic transport condition. Another method which disrupts the direct metal-2D material interactions by inserting a hexagonal boron nitride or graphene layer in between, was found to effectively reduce the barrier height[24,25]. We check this method by inserting a single graphene layer between the Au or Pt and WSe_2 layers and the corresponding configuration is Au/Pt-G-WSe_2-G-Au/Pt. Another benefit for this configuration is that introducing graphene could lead to clean interfaces while reducing the thermal conduction further due to the phonon interface scattering. The barrier heights for both Au and Pt covered by graphene show significant reduction compared to those of the pure metal. In particular, the p-type barrier height is found to be only 0.04 eV and 0.02 eV for 3 and 5 layers of WSe_2, respectively, sandwiched within the Pt/G electrodes. The barrier height is on the order of k_BT, so Pt-G-WSe_2-G-Pt is a promising p-type candidate for high-performance solid-state thermionic devices.

For the n-type device, first we evaluate the configuration of Sc-WSe_2-Sc, since Sc has a very low work function of 3.5 eV. The calculated n-type barrier height for the 4 layer WSe_2 is 0.17 eV which is too high for thermionic energy conversion. Inserting a graphene layer between the Sc and WSe_2 didn't show any reduction of the barrier height. A usual way to reduce the Schottky barrier height for conventional metal-semiconductor junctions is through doping. Instead of applying ionic substitutional doping, we find the 2D transition metal dichalcogenide (TMD) family have a staggered band alignment[26], so charge transfer doping could be obtained by stacking two or more of the TMD layers. $MoSe_2$ is used for this purpose since the lattice matches that of WSe_2, which is favored for the calculations due to the small in-plane supercell. In particular, we evaluate the configuration of Sc-WSe_2-$MoSe_2$-WSe_2-Sc. For 4 layer $MoSe_2$, the calculated barrier height is 0.03 eV which is as promising as that of the p-type Pt-G-WSe_2-G-Pt. The above discussions are based on the DFT results. In what follows, we show the more accurate GW calculations and the thermionic energy conversion performance of one of the two promising configurations, namely, the Sc-WSe_2-$MoSe_2$-WSe_2-Sc, due to its smaller supercell size.

Quasiparticle band structure. The DFT and *GW* band structures of the scattering region of the proposed Sc-WSe_2-$MoSe_2$-WSe_2-Sc device are shown in Fig. 1(b) and (c) respectively. The fatbands of the WSe_2 layers (red lines) are significantly distorted from the ideal isolated bands[27], indicating strong hybridization of the wave functions of WSe_2 and Sc. This is the result of the short distance of 2.0 Å between Sc and the contacting Se. The band structure of the $MoSe_2$ layers (blue lines) are well reproduced[27], resembling the van der Waals bonding nature. The indirect bandgap from Γ to Q, of the central quadlayer $MoSe_2$ was calculated to be 0.90 eV and 1.11 eV and the values for the direct bandgap at K are 1.38 eV and 1.65 eV using DFT and *GW* calculations, respectively. Normally, *GW* predicts much larger bandgap than DFT for 2D materials, e.g., around 1 eV, 0.7 eV, and 0.5 eV larger for monolayer, bilayer, and bulk MoS_2, respectively[27–30]. Such small correction for the present structure, i.e., 0.2–0.3 eV, reminds us of the significant bandgap renormalization due to the substrate screening effect[19,20]. Note that the renormalization is substrate dependent, e.g., the bandgap of MoS_2 is reduced by almost 1 eV on Au substrate[20], while the reduction is only 0.13 eV for $MoSe_2$ on bilayer graphene[19]. In the proposed device configuration, the dynamic screening effect is more effective and significant[31], due to both higher screening of the sandwiched structure compared to MoS_2 on a substrate (single sided) and the presence of metallic electrodes with substantially higher density of electrons compared to the graphene electrodes.

The Fermi level E_F is located near the conduction bands of $MoSe_2$, as shown in Fig. 1(b) and (c), which means $MoSe_2$ is n-type doped. We find that the *GW* correction on the transport barrier height is valley dependent. For

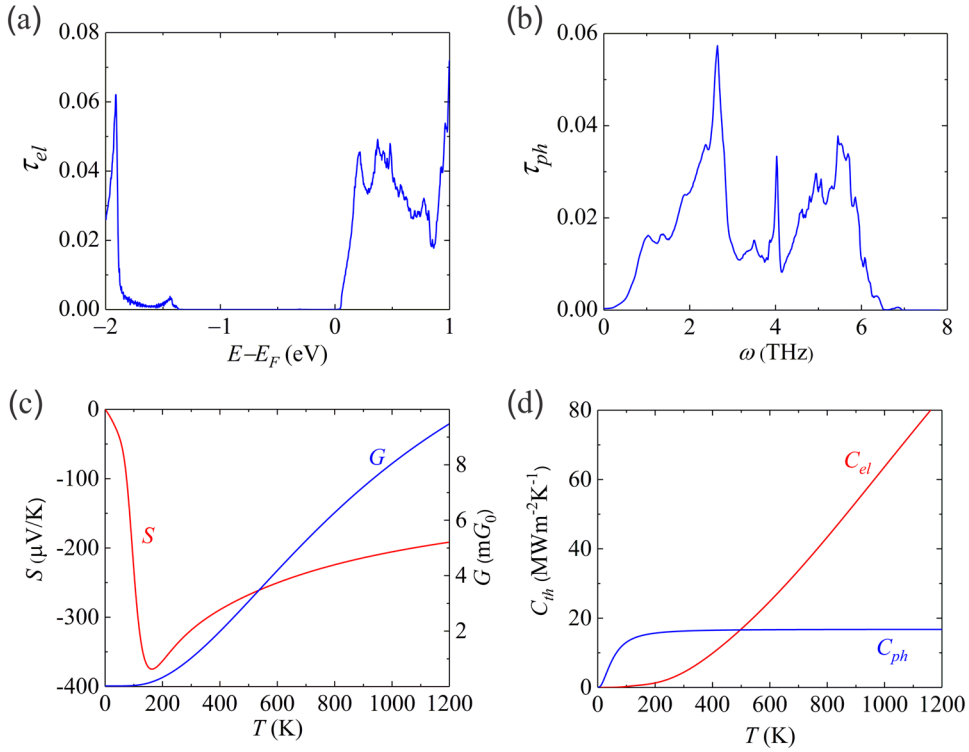

Figure 2. Thermionic transport properties of the proposed 2D vdWH device. (**a**) Electron transmission function τ_{el}, (**b**) phonon transmission function τ_{ph}, (**c**) Seebeck coefficient S and electrical conductance G, (**d**) thermal conductance C_{th}. ω is the phonon frequency and T is the absolute temperature. $G_0 = 2e^2/h$ is the electrical conductance quantum.

the K valley, the barrier height is changed from 0.20 eV of DFT to 0.33 eV of *GW*. However, for the Q valley, the correction is only 0.03 eV, i.e., from 0.03 eV to 0.06 eV. Since the large energy difference between the K and Q valleys compared to k_BT, the transport property is dominated by the Q valley. Figure 1(d) shows the *GW* LDOS at each layer. The white area with LDOS of zero is located in the central MoSe2 layers. It spans about 1 eV along the vertical axis, which represents the bandgap of MoSe2. The WSe_2 layers show metallic behavior as a result of significant wave function hybridizations with Sc. The thermionic transport barrier E_b is determined by the middle $MoSe_2$ layers.

Thermionic transport properties. Figure 2(a) displays the electron transmission function τ_{el} of the proposed vdWH device. There is a sharp slope of τ_{el} with respect to energy at 0.06 eV above E_F. This slope is due to the Q valley states of the $MoSe_2$ layers, consistent with the band structures. In the case of thermoelectric materials, it is known that sharp slopes of the differential conductivity with respect to energy results in asymmetry in electron-hole transport and therefore enhances the Seebeck coefficient. Similarly, sharp slopes of τ_{el} curve favors the thermionic energy conversion by increasing the asymmetry between low and high energy electrons or in other words by acting as an effective barrier to filter out the low energy electrons. On the hole side, τ_{el} arises at 1.3 eV below E_F. From Fig. 1(c), we know that the valence band maximum (VBM) of the $MoSe_2$ layers is located at 1 eV and 1.3 eV below E_F at Γ and K, respectively. Therefore, the holes at Γ do not contribute to the transmission, which can be understood from the small LDOS shown in Fig. 1(d). The τ_{el} is the electrical conductance G at zero temperature. At higher temperatures, electrons have higher kinetic energies and more electrons in Sc can be emitted to the $MoSe_2$ conduction bands overcoming the barrier E_b, contributing to the increase of G, as shown in Fig. 2(c). The n-type doping of the vdWH can be further verified by the negative sign of the Seebeck coefficient S. We obtained a maximum S of 375 μVK^{-1} at 160 K, while the room temperature value is 320 μVK^{-1}.

The phonon transmission function τ_{ph} is shown in Fig. 2(b). The cutoff frequency ω_c of τ_{ph} is determined by the smallest ω_c of the components since three-phonon scattering was not considered. The ω_c of the Sc, WSe_2, and $MoSe_2$ layers are 7.5 THz, 8.2 THz, and 10.4 THz, respectively, as determined by the phonon projected DOS (see Figure S1), in agreement with the literature[32–34]. Hence, in the present structure, the highest phonon transport channels are determined by Sc. The phonon thermal conductance C_{ph} is saturated at 16 MW m^{-2} K^{-1} above 200 K, as shown in Fig. 2(d). This ideal value is four times larger than that of similar configuration of graphene-phosphorene-graphene sandwiched by gold electrodes[10]. This is because gold has lower ω_c of 4.7 THz[35] and there is larger acoustic mismatch in that structure. The electron thermal conductance C_{el} increases following the trend of G as the temperature increased. At room temperature, phonons dominate the thermal transport, until above 500 K, when C_{el} becomes larger.

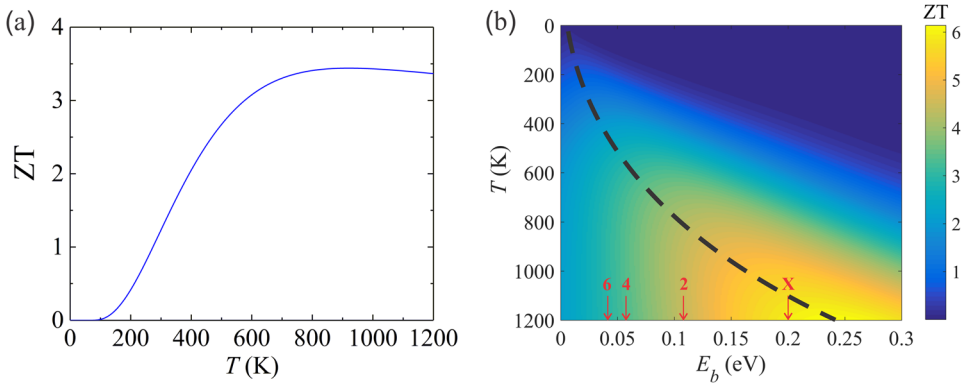

Figure 3. (**a**) The figure of merit ZT of the proposed device. (**b**) Contour plot of ZT as a function of thermionic barrier height E_b and temperature T. Energy barrier values labeled by 2, 4, and 6 correspond to different number (n) of $MoSe_2$ layers in Sc-WSe_2-n$MoSe_2$-WSe_2-Sc. Label X is for Sc-4$MoSe_2$-Sc. The dashed line shows the position of optimum barrier height leading to maximum efficiency at various temperatures.

We also show the equivalent figure of merit ZT in Fig. 3(a), defined as $ZT = GS^2T/(C_{el} + C_{ph})$, to compare with thermoelectric materials. The obtained room temperature ZT is 1.2 which is competitive to the commercial thermoelectric materials with ZT around unity. The ZT increases above 3 at 600 K and reaches a maximum value of 3.4 at 800 K. The experimental record ZT is 2.6 obtained for SnSe at 923 K[36]. Hence, our proposed device is very promising for energy conversion. Since the transport barrier E_b can be tuned by changing the number of $MoSe_2$ layers, we plot ZT at varied E_b assuming the same C_{ph} and shifted τ_{el}, as shown in Fig. 3(b). This approximation was verified by explicitly calculating the transport properties of the WSe_2–2$MoSe_2$-WSe_2 structure sandwiched by Sc. The E_b of the bilayer $MoSe_2$ from GW calculation is 0.11 eV, also 0.03 eV larger than that of DFT. The calculated C_{ph} is 15 MW m^{-2} K^{-1} which is only 1 MW m^{-2} K^{-1} smaller than that of the quadlayer case (see Figure S2). The room temperature ZT is 0.5 which agrees with the plot in Fig. 3(b). For the hexalayer $MoSe_2$, the E_b is 0.04 eV after applying a GW correction of 0.03 eV (see Figure S3). We label these structures of Sc-WSe2-nMoSe2-WSe2-Sc with the number (n) of the MoSe2 layers in Fig. 3(b). For solid-state thermionic transport, the general constraint on the barrier width ℓ is $\ell_t < \ell < \lambda$, where λ is the electron mean free path and ℓ_t is the minimum thickness to prevent the electron from tunneling through the barrier[1]. For the present structure with 6 layers of $MoSe_2$, we have $\ell = 4.8$ nm, smaller than typical λ of 5–10 nm for most semiconductors. For the bilayer $MoSe_2$ with $\ell = 2.4$ nm, however, we found electron tunneling (see Figure S4) will degrade the device performance. As shown by the dashed line in Fig. 3(b), the optimum barrier height for the maximum ZT increases as the temperature increased. Label X is for Sc-4MoSe2-Sc which has a E_b of 0.2 eV and a C_{ph} of 19 MW m^{-2} K^{-1} (see Figures S5 and S2). This structure has a large ZT at very high temperature but nearly zero at room temperature. Note that our calculations are based on ballistic transport regime which may not be valid at very high temperatures.

Thermionic refrigeration. We also propose the present vdWH as a thermionic refrigerator. The working principle is shown in Fig. 4(a). A bias V is applied with the chemical potentials $\mu_R > \mu_L$ to pump heat J_Q from right to left. As a result of this heat flow a temperature difference ΔT is established between left and right, causing a heat back flow of $C_{ph}\Delta T$. The cooling coefficient of performance (COP) is defined as the heat coming out of the cold side divided by the input electrical work: $COP = (J_Q - C_{ph}\Delta T)/JV$, where J is the electrical current. We have shown that COP can be evaluated from first-principles[10]. We define the cooling efficiency normalized by the Carnot COP for cooling ($COP_C = T_C/\Delta T$) as $\eta = COP/COP_C$. The optimum efficiency η_{max} obtained for the optimum E_b at different working temperatures is shown in Fig. 4(b). η_{max} follows the same trend as ZT shown in Fig. 3(a). Over 30% of the Carnot efficiency is achieved with the temperature above 450 K. The efficiency changes slightly as ΔT increases. At room temperature, η_{max} increases from 19.45% to 19.89% as ΔT increases from 5 K to 40 K.

For thermoelectric materials, the relation between ZT and the efficiency of thermoelectric cooling[1] is $(\gamma T_C - T_H)/[\Delta T(\gamma + 1)]$ so that the cooling efficiency with respect to Carnot becomes $\eta_{TE} = (\gamma - T_H/T_C)/(\gamma + 1) \approx (\gamma - 1)/(\gamma + 1)$, where $\gamma = \sqrt{1 + ZT}$. Take the room temperature ZT of 1.2 of the present structure and ΔT of 1 K, we obtain a η_{TE} of 19.3%, almost equal to the thermionic η_{TI} of 19.4% obtained from the definition of COP under the same condition. We use this argument to show that the "ballistic" ZT of the thermionic device, which includes the contacts to leads, using the standard definition of the efficiency[1] leads to almost the same efficiency directly derived from the COP introduced a few lines above. In this sense, the "ballistic" ZT leads to a consistent comparison with thermoelectrics ZT. We also compared our first-principles results with those obtained based on Richardson's law[1,2] taking the calculated E_b of 0.06 eV and C_{ph} of 16 MW m^{-2} K^{-1} as input. We assumed the averaged electron transmission $\overline{\tau} = 1$ and the electron effective mass $m^* = 1$ in the Richardson constant A. As can be seen from the Fig. 4(b), the overall agreement is satisfactory. We note that this agreement is fortuitous since the perfect electron transmission is assumed in the Richardson equation. In reality, $\overline{\tau}$ should be smaller than 1 due to the back-scattering of the electron waves at the interface and the existence of the barrier; therefore the effective mass must be greater than 1 to

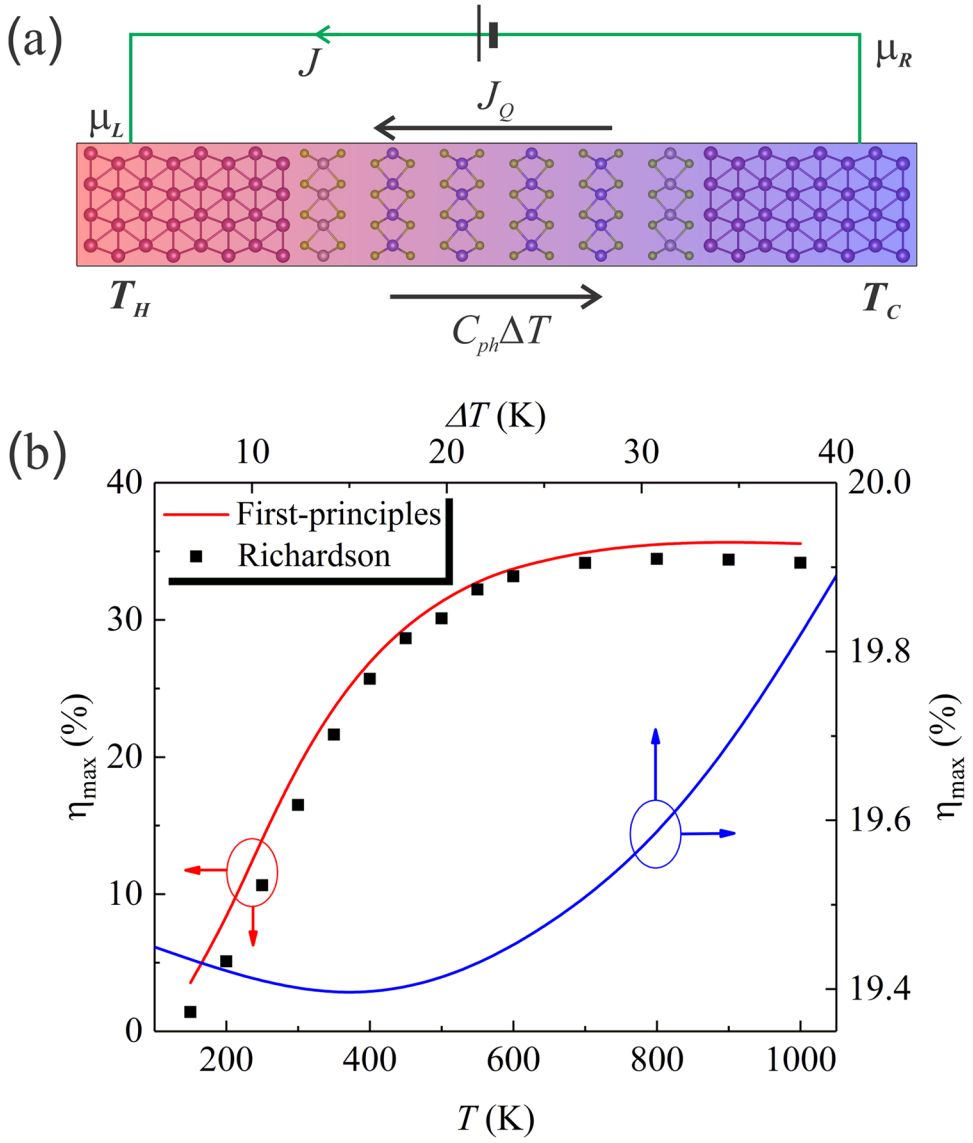

Figure 4. (**a**) Schematic configuration shows the working principle of the proposed device as a thermionic refrigerator. Arrows indicate the charge or energy flow directions. J, J_Q, $C_{ph}\Delta T$, μ, and T are electrical current, electron (carriers) thermal current, phonon thermal current, chemical potential, and temperature, respectively. (**b**) Maximum cooling efficiency of the proposed device. The red curve was obtained by fixing the temperature difference ΔT to 5 K while varying the hot side temperature T_H. For the blue curve, $T_H = 300$ K was fixed while varying ΔT. The data calculated based on the Richardson's law with $\overline{\tau} = 1$, $m^* = 1$, $E_b = 0.06$ eV, and $C_{ph} = 16\,\mathrm{MW\,m^{-2}\,K^{-1}}$, were shown as black squares.

reproduce the first-principles results. We note that the device could be further optimized by engineering the phonon thermal conductance, e.g., by introducing lattice mismatch or disorder, since the room temperature thermal conductance is dominated by phonons as shown in Fig. 3(d).

In summary, we have shown how simple design principles and use of accurate first principles calculations, could lead to high-performance for solid-state vdWH thermionic energy conversion devices. we proposed two promising devices, namely, the p-type Pt-G-WSe_2-G-Pt and n-type Sc-WSe_2-$MoSe_2$-WSe_2-Sc. The performance of the latter is characterized by more accurate GW and real space Green' function calculations. We find even though the *GW* correction due to the large dynamic screening effect from the Sc electrodes to the barrier is small, in absolute value (0.03 eV), it still is on the order of the energy barrier itself, and thus strongly affects the thermionic current. The proposed structure has a room temperature ZT of 1.2 which increases to 3 above 600 K. A high performance with cooling efficiency over 30% of the Carnot efficiency above 450 K is predicted. Our findings show that vdWHs with appropriate electrodes have great potential when used in thermionic energy conversion devices.

Methods

DFT calculation. The DFT calculations were performed using the Quantum Espresso package[37]. SG15 norm-conserving pseudopotentials[38], PBE[39] exchange correlation functional, kinetic energy cutoff of 60 Ry, and a k mesh of $12 \times 12 \times 1$ were used. Lattice was relaxed with the force on each atom less than 1.0e-4 Ry/Bohr. We first optimized separately the lattices of Sc, WSe_2, and $MoSe_2$. The optimized in-plane lattice constants are 3.319 Å, 3.320 Å, and 3.320 Å, respectively. We then constructed the vdWH including the electrodes with AB stacking by fixing the in-plane lattice constant of 3.319 Å across all the layers. In this configuration, there are almost no in-plane strains on any layer. With the in-plane lattice constant fixed, we further optimized the whole structure using optB86 functional[40] to include the vdW correlations. The optimized interlayer distances of $MoSe_2$-$MoSe_2$ and $MoSe_2$-WSe_2 are 6.5 Å. The relaxed coordinates can be found in supplementary files. DFT band structure calculations were performed on the relaxed structure but with PBE functional. Spin-orbit coupling (SOC) was not included since the effect is less important for Mo than W, given that the thermionic barrier is determined by the $MoSe_2$ layer. Moreover, SOC is less important for CBM than for VBM. Even for the CBM, the Q valley is less affected than the K valley (see Figure S6). Fatbands were calculated using the maximally localized Wannier functions (MLWFs) as implemented in the wannier90 code[41]. Initial projections for Sc, Se, W, and Mo atoms were chosen as (d; sp^3-1), p, d, d, respectively.

***GW* calculation.** Single-shot GW or G_0W_0 calculations based on PBE wave functions were performed using the ABINIT code[42,43]. SG15 norm-conserving pseudopotentials, wave function cutoff of 60 Ry, dielectric matrix cutoff ϵ_C of 10 Ry, exchange self-energy cutoff of 240 Ry, 1500 bands for both the dielectric matrix and self-energy calculations, and a k mesh of $9 \times 9 \times 1$ were used. We included 4 layers of Sc at each side (total 8 layers) in the GW calculation. The transport barrier did not change with 8 more Sc layers added. The contour deformation method with 10 grids on the imaginary axis, 20 grids on the real axis, and the cutoff frequency of 1 Ry was used to calculate the dielectric matrix and self-energy. Further increasing the imaginary axis grid to 20 and real axis grid to 50 changed the results by less than 1%. GW calculations highly depend on the convergence of the parameters, of which the most important are k mesh, ϵ_C, and the number of bands (nbands). The latter two are interdependent. We checked the convergence of k mesh with $\epsilon_C = 10$ Ry, nbands = 500, and plasmon-pole model used. Increasing the k mesh from $9 \times 9 \times 1$ to $12 \times 12 \times 1$ changed the barrier height by only 3 meV. The convergence of ϵ_C and nbands were checked with k meshes of $3 \times 3 \times 1$ and $6 \times 6 \times 1$ (see Figure S7). The accuracy with error within 0.01 eV can be obtained with $\epsilon_C = 20$ Ry and nbands = 3000. However, using these values for the $9 \times 9 \times 1$ k mesh is computationally prohibitive. We found that the convergence curves at different k meshes with the same ϵ_C are quite similar. Therefore, we first evaluated the barriers with $\epsilon_C = 10$ Ry, nbands = 1500, and $\epsilon_C = 20$ Ry, nbands = 3000 for k mesh of $6 \times 6 \times 1$. The corresponding barrier heights are b_1 and b_2. We then calculated the barrier height b_3 with $\epsilon_C = 10$ Ry and nbands = 1500 for k mesh of $9 \times 9 \times 1$. The final correct barrier height was estimated using $b_3 + b_2 - b_1$. For our present calculations, we found that the correction $b_2 - b_1$ was very small, i.e., −0.03 eV. Thus we used the result from $\epsilon_C = 10$ Ry and nbands = 1500 to plot the band structure, but the corrected bands were used in the transport calculations. The GW band structure was generated using the MLWFs.

Electron transport. We used the real space Green's function method[44,45] with localized basis Hamiltonian constructed using MLWFs to calculate the ballistic electron transport. The retarded Green's function of the scattering region reads:

$$\boldsymbol{G}^r = [(\varepsilon + i\delta)\boldsymbol{I} - \boldsymbol{H} - \boldsymbol{\Sigma}_L - \boldsymbol{\Sigma}_R]^{-1} \tag{1}$$

where $\boldsymbol{I}$ the identity matrix, ε the electron energy, $i\delta$ is a small imaginary number. $\boldsymbol{\Sigma}_{L,R}$ denotes the self-energy of the left (L) or right (R) lead. $\boldsymbol{H}$ is the scattering region Hamiltonian, on which we imposed a minor scissor correction of 0.03 eV to take the GW correction into account. The electron transmission function is $\tau_{el} = \mathrm{Tr}(\boldsymbol{G}^r \boldsymbol{\Gamma}_L \boldsymbol{G}^a \boldsymbol{\Gamma}_R)$, where $\boldsymbol{G}^a = (\boldsymbol{G}^r)^\dagger$ is the advanced Green's function and $\boldsymbol{\Gamma}_{L/R} = i(\boldsymbol{\Sigma}_{L/R} - \boldsymbol{\Sigma}_{L/R}^\dagger)$. Note that the above method is used for 1D transport. For the case of 3D transport, one samples the 2D Brillouin zone perpendicular to the transport direction with a fine k mesh. For each transverse k point, the k-dependent transmission $\tau_{el}(\varepsilon, k)$ should be calculated and the total transmission would be $\tau_{el}(\varepsilon) = \sum_k \tau_{el}(\varepsilon, k) w_k$, where w_k is the k point weight. In the present calculation, we used a k grid of $150 \times 150 \times 1$ to obtain a smooth transmission function. The electron transmission was calculated using the WanT code[46]. With τ_{el}, one can obtain the coherent transport coefficients under the linear response approximation[47]:

$$G = e^2 L_0 \tag{2}$$

$$S = L_1/(eTL_0) \tag{3}$$

$$\kappa_{el} = (L_2 - L_1^2/L_0)/T \tag{4}$$

$$L_n = 2/h \int d\varepsilon \tau_{el}(\varepsilon) \times (\varepsilon - \mu)^n \times (-\partial f/\partial \varepsilon) \tag{5}$$

where f is the Fermi-Dirac distribution function. The two-probe electrical current and electron thermal current are:

$$J = 2e/h \int d\varepsilon \tau_{el}(\varepsilon)(f_L - f_R) \tag{6}$$

$$J_Q = 2/h \int d\varepsilon \tau_{el}(\varepsilon)(\varepsilon - \mu)(f_L - f_R) \tag{7}$$

We can impose any two of the four quantities (J, J_Q, ΔT, $\Delta\mu$) and obtain the remaining two from the above two equations.

Phonon transport. The phonon Green's function method[48,49] was used to calculate the ballistic phonon transport. The equations to calculate the phonon transmission function τ_{ph} are similar to those of the electron transport. One only needs to substitute ε by ω^2 and $\boldsymbol{H}$ by $\boldsymbol{\Phi}$, where $\boldsymbol{\Phi}$ is the interatomic force constant matrix divided by atomic masses. The phonon thermal conductance was calculated as:

$$C_{ph} = \hbar/2\pi \int d\omega \omega \tau_{ph}(\omega)(\partial n/\partial T) \tag{8}$$

where n is the Bose-Einstein distribution function. We used the finite difference method as implemented in the SIESTA code[50] to calculate the interatomic force constant matrix. A $3 \times 3 \times 1$ supercell was constructed and the displacement was 0.01 Å for each degree of freedom. Troullier-Martins pseudopotentials[51], double zeta plus polarization basis set, PBE exchange correlation functional, a $6 \times 6 \times 1$ k mesh, energy shift of 50 meV, and real space grid cutoff of 300 Ry were used for the supercell calculations. With the calculated interatomic force constant matrix as input, the phonon transmission was calculated using the transport module of the WanT code. The phonon PDOS was evaluated using the Phonopy code[52].

References

1. Mahan, G. D., Sofo, J. O. & Bartkowiak, M. Multilayer thermionic refrigerator and generator. *J. Appl. Phys.* **83**, 4683–4689 (1998).
2. Mahan, G. D. & Woods, L. M. Multilayer Thermionic Refrigeration. *Phys. Rev. Lett.* **80**, 4016–4019 (1998).
3. Shakouri, A. & Bowers, J. E. Heterostructure integrated thermionic coolers. *Appl. Phys. Lett.* **71**, 1234–1236 (1997).
4. Vining, C. B. & Mahan, G. D. The B factor in multilayer thermionic refrigeration. *J. Appl. Phys.* **86**, 6852–6853 (1999).
5. Ulrich, M. D., Barnes, P. A. & Vining, C. B. Comparison of solid-state thermionic refrigeration with thermoelectric refrigeration. *J. Appl. Phys.* **90**, 1625–1631 (2001).
6. Zebarjadi, M. Solid-State Thermionic Power Generators: An Analytical Analysis in the Nonlinear Regime. *Phys. Rev. Appl.* **8**, 1–7 (2017).
7. Mahan, G. D. Thermionic refrigeration. *J. Appl. Phys.* **76**, 4362–4366 (1994).
8. Geim, A. K. & Grigorieva, I. V. Van der Waals heterostructures. *Nature* **499**, 419–425 (2013).
9. Novoselov, K. S., Mishchenko, A., Carvalho, A. & Castro Neto, A. H. 2D materials and van der Waals heterostructures. *Science* (80−). **353**, aac9439 (2016).
10. Wang, X., Zebarjadi, M. & Esfarjani, K. First principles calculations of solid-state thermionic transport in layered van der Waals heterostructures. *Nanoscale* **8**, 14695–14704 (2016).
11. Massicotte, M. *et al*. Photo-thermionic effect in vertical graphene heterostructures. *Nat. Commun.* **7**, 12174 (2016).
12. Liang, S.-J., Liu, B., Hu, W., Zhou, K. & Ang, L. K. Thermionic Energy Conversion Based on Graphene van der Waals Heterostructures. *Sci. Rep.* **7**, 46211 (2017).
13. Chen, C. C., Li, Z., Shi, L. & Cronin, S. B. Thermoelectric transport across graphene/hexagonal boron nitride/graphene heterostructures. *Nano Res.* **8**, 666–672 (2015).
14. Poudel, N. *et al*. Cross-plane Thermoelectric and Thermionic Transport across Au/h-BN/Graphene Heterostructures. *Sci. Rep.* **7**, 14148 (2017).
15. Rasmussen, F. A. & Thygesen, K. S. Computational 2D Materials Database: Electronic Structure of Transition-Metal Dichalcogenides and Oxides. *J. Phys. Chem. C* **119**, 13169–13183 (2015).
16. Cai, Y., Zhang, G. & Zhang, Y.-W. Layer-dependent Band Alignment and Work Function of Few-Layer Phosphorene. *Sci. Rep.* **4**, 6677 (2015).
17. Kim, C. *et al*. Fermi Level Pinning at Electrical Metal Contacts of Monolayer Molybdenum Dichalcogenides. *ACS Nano* **11**, 1588–1596 (2017).
18. Andersen, K., Latini, S. & Thygesen, K. S. Dielectric Genome of van der Waals Heterostructures. *Nano Lett.* **15**, 4616–4621 (2015).
19. Ugeda, M. M. *et al*. Giant bandgap renormalization and excitonic effects in a monolayer transition metal dichalcogenide semiconductor. *Nat. Mater.* **13**, 1091–1095 (2014).
20. Bruix, A. *et al*. Single-layer MoS2 on Au(111): Band gap renormalization and substrate interaction. *Phys. Rev. B* **93**, 165422 (2016).
21. Garcia-Lastra, J. M., Rostgaard, C., Rubio, A. & Thygesen, K. S. Polarization-induced renormalization of molecular levels at metallic and semiconducting surfaces. *Phys. Rev. B* **80**, 245427 (2009).
22. Hybertsen, M. S. & Louie, S. G. Electron correlation in semiconductors and insulators: Band gaps and quasiparticles energies. *Phys Rev B* **34**, 5390 (1986).
23. Chiritescu, C. *et al*. Ultralow thermal conductivity in disordered, layered WSe2 crystals. *Science* **315**, 351–353 (2007).
24. Farmanbar, M. & Brocks, G. Ohmic Contacts to 2D Semiconductors through van der Waals Bonding. *Adv. Electron. Mater.* **2**, 1500405 (2016).
25. Farmanbar, M. & Brocks, G. Controlling the Schottky barrier at MoS2/metal contacts by inserting a BN monolayer. *Phys. Rev. B* **91**, 161304 (2015).
26. Gong, C. *et al*. Band alignment of two-dimensional transition metal dichalcogenides: Application in tunnel field effect transistors. *Appl. Phys. Lett.* **103**, 0–4 (2013).
27. Roldán, R. *et al*. Electronic properties of single-layer and multilayer transition metal dichalcogenides MX 2 (M = Mo, W and X = S, Se). *Ann. Phys.* **526**, 347–357 (2014).
28. Kormányos, A. *et al*. K.P Theory for Two-Dimensional Transition Metal Dichalcogenide. *Semiconductors. 2D Mater.* **2**, 22001 (2014).
29. Cheiwchanchamnangij, T. & Lambrecht, W. R. L. Quasiparticle band structure calculation of monolayer, bilayer, and bulk MoS2. *Phys. Rev. B* **85**, 205302 (2012).
30. Jiang, H. Electronic Band Structures of Molybdenum and Tungsten Dichalcogenides by the GW Approach. *J. Phys. Chem. C* **116**, 7664–7671 (2012).
31. Ryou, J. & Kim, Y.-S. KC, S. & Cho, K. Monolayer MoS2 Bandgap Modulation by Dielectric Environments and Tunable Bandgap Transistors. *Sci. Rep.* **6**, 29184 (2016).

32. Pleschiutschnig, J., Blaschko, O. & Reichardt, W. Phonon dispersion and heat capacity of scandium. *Phys. Rev. B* **44**, 6794–6798 (1991).
33. Horzum, S. *et al*. Phonon softening and direct to indirect band gap crossover in strained single-layer MoSe2. *Phys. Rev. B* **87**, 125415 (2013).
34. Terrones, H. *et al*. New First Order Raman-active Modes in Few Layered Transition Metal Dichalcogenides. *Sci. Rep.* **4**, 4215 (2015).
35. Lynn, J. W., Smith, H. G. & Nicklow, R. M. Lattice dynamics of gold. *Phys. Rev. B* **8**, 3493–3499 (1973).
36. Zhao, L.-D. *et al*. Ultralow thermal conductivity and high thermoelectric figure of merit in SnSe crystals. *Nature* **508**, 373–377 (2014).
37. Giannozzi, P. *et al*. QUANTUM ESPRESSO: a modular and open-source software project for quantum simulations of materials. *J. Phys. Condens. Matter* **21**, 395502 (2009).
38. Schlipf, M. & Gygi, F. Optimization algorithm for the generation of ONCV pseudopotentials. *Comput. Phys. Commun.* **196**, 36–44 (2015).
39. Perdew, J. P., Ernzerhof, M. & Burke, K. Rationale for mixing exact exchange with density functional approximations. *J. Chem. Phys.* **105**, 9982–9985 (1996).
40. Klimeš, J., Bowler, D. R. & Michaelides, A. Van der Waals density functionals applied to solids. *Phys. Rev. B* **83**, 195131 (2011).
41. Mostofi, A. A. *et al*. An updated version ofwannier90: A tool for obtaining maximally-localised Wannier functions. *Comput. Phys. Commun.* **185**, 2309–2310 (2014).
42. Gonze, X. A brief introduction to the ABINIT software package. *Zeitschrift für Krist. - Cryst. Mater.* **220**, 558–562 (2005).
43. Gonze, X. *et al*. ABINIT: First-principles approach to material and nanosystem properties. *Comput. Phys. Commun.* **180**, 2582–2615 (2009).
44. Nardelli, M. B. Electronic transport in extended systems: Application to carbon nanotubes. *Phys. Rev. B* **60**, 7828–7833 (1999).
45. Datta, S. Nanoscale device modeling: the Green's function method. *Superlattices Microstruct.* **28**, 253–278 (2000).
46. Ferretti, A., Bonferroni, B., Calzolari, A. & Nardelli, M. B. WanT code. Available at: http://www.wannier-transport.org.
47. Esfarjani, K., Zebarjadi, M. & Kawazoe, Y. Thermoelectric properties of a nanocontact made of two-capped single-wall carbon nanotubes calculated within the tight-binding approximation. *Phys. Rev. B* **73**, 85406 (2006).
48. Wang, J. S., Wang, J. & Zeng, N. Nonequilibrium Green's function approach to mesoscopic thermal transport. *Phys. Rev. B* **74**, 2–5 (2006).
49. Mingo, N. & Yang, L. Phonon transport in nanowires coated with an amorphous material: An atomistic Green's function approach. *Phys. Rev. B* **68**, 245406 (2003).
50. Soler, J. M. *et al*. The SIESTA method for ab initio order- N materials. *J. Phys. Condens. Matter* **2745**, 2745–2779 (2002).
51. Troullier, N. & Martins, J. L. Efficient pseudopotentials for plane-wave calculations. *Phys. Rev. B* **43**, 1993–2006 (1991).
52. Togo, A. & Tanaka, I. First principles phonon calculations in materials science. *Scr. Mater.* **108**, 1–5 (2015).

Acknowledgements

The authors wish to acknowledge SOE HPC cluster of Rutgers, Rivanna cluster of UVA, and XSEDE, which is supported by National Science Foundation grant number ACI-1053575, for providing the computation resources. This work is supported by National Science Foundation, grant numbers 1400246 (X.W. and M.Z.) and 1403089 (X.W. and K.E.).

Author Contributions

K.E. and M.Z. defined the problem. X.W. performed the calculations and wrote the paper. All authors contributed to the final version and the presentation of the paper.

Additional Information

Supplementary information accompanies this paper at https://doi.org/10.1038/s41598-018-27430-0.

Competing Interests: The authors declare no competing interests.

Publisher's note: Springer Nature remains neutral with regard to jurisdictional claims in published maps and institutional affiliations.

Open Access This article is licensed under a Creative Commons Attribution 4.0 International License, which permits use, sharing, adaptation, distribution and reproduction in any medium or format, as long as you give appropriate credit to the original author(s) and the source, provide a link to the Creative Commons license, and indicate if changes were made. The images or other third party material in this article are included in the article's Creative Commons license, unless indicated otherwise in a credit line to the material. If material is not included in the article's Creative Commons license and your intended use is not permitted by statutory regulation or exceeds the permitted use, you will need to obtain permission directly from the copyright holder. To view a copy of this license, visit http://creativecommons.org/licenses/by/4.0/.

© The Author(s) 2018